Vertex reconstruction in hyperons decays.

Facility for Antiproton and Ion Research in Europe and
GSI Helmholtzzentrum fur Schwerionenforschung

ADAM STRACH

Internship and Training Project Report
Darmstadt, Germany
25-10-2022

GET INvolved 2022: 221019S (GI18-PL-STP)

Copyrights(c)
Personal use of this material is permitted. However, permission to reprint/republish this material for advertising or promotional purposes or for creating new collective works for resale or redistribution to servers or lists, or to reuse any copyrighted component of this work in other works must be obtained from the GSI GmbH and FAIR GmbH.

Author(s)
Adam Strach
Jagiellonian University, Faculty of Physics,
Astronomy and Applied Computer Science
ul. prof. Stanisława Łojasiewicza 11, Kraków
Email: Adam.strach@student.uj.edu.pl

Project Mentor/Supervisor
Dr. Johan Messchendorp
FFN
GSI Helmholtzzentrum für Schwerionenforschung GmbH,
Planckstr. 1, 64291 Darmstadt, Germany
Tel: +49 6159 71 3556
Email: j.messchendorp@gsi.de

Program Coordinator
Dr. Pradeep Ghosh
GSI Helmholtzzentrum für Schwerionenforschung GmbH &
Facility for Antiproton and Ion Research in Europe GmbH
Tel: +49 6159 71 3257, Fax: +49 6159 71 3916
Email: Pradeep.Ghosh@fair-center.eu

https://www.overleaf.com/project/6302479b5e5a218e218c53e7 **GET Involved 2022: GI-221019S-PL-STP**

Publisher: GSI Helmholtzzentrum für Schwerionenforschung GmbH,
Planckstr. 1, 64291 Darmstadt, Germany
Published: September 2022

Abstract

I have analyzed proton-proton elastic interactions and the $pp \to p\pi^+\Lambda K_S^0$ channel using a kinematic fitting procedure prepared for the HADES experiment. The analysis of the proton-proton elastic scattering channel gave unsatisfactory results and requires further work. For the ΛK_S^0 channel, I have performed three vertex fits: the Λ and K_S^0 decay vertices as well as the primary vertex respectively. We concluded that vertex fit works well for that channel. I was able to observe peaks in the reconstructed mass spectrum corresponding to decays of the Λ and K_S^0 hadrons. I have tested the kinematic fitter ability for selection of the Λ decay product particles, by doing probability cuts on Λ vertex probability and the full interaction probability. Without any cuts, around 29.7% Λ and 28.8% K_S^0 decay products were selected correctly. It was observed that the Λ efficiency can be improved by optimizing the convergence criterion, and probability cuts. In addition to the vertex fit further constraints can also be tested for the Λ selection.

Declaration

I hereby declare that the project entitled "**Vertex reconstruction in hyperons decays**" is my own work and that I have correctly acknowledged the work of others.

Acknowledgements

I would like to thank my supervisors: Dr. Johan Messchendorp and
Dr. Jenny Regina for taking care of me during my practises, and for all the help and explanation they patiently gave me.
I would like to thank Dr. Jenny Regina, Dr. Waleed Esmail, Jana Rieger and other people that developed or have helped to develop kinematic fitting for HADES.
I am also thankful to Prof. James Ritman for suggestion on changing track parametriation to improve resolution in the Z parameter in the Forward Tracker.

Contents

1 Introduction **12**
1.1 Brief overview of report structure 12
1.2 Hyperons and their importance 12
1.3 The HADES experiment 13
1.4 The PANDA experiment and the HADES Forward Detector . 15
1.5 Tracking of particles in experiments 17
1.6 Kinematic Refit 18
1.6.1 Track parametrization 19
1.6.2 Vertex constraint 19
1.6.3 4-Constraint 20
1.6.4 3-Constraint 20

2 Analysis **21**
2.1 Analyzed reaction channels 21
2.2 Elastic proton-proton interaction 23
2.2.1 Obtaining variances of parameters 23
2.2.2 Forward-main HADES elastic proton-proton analysis 24
2.2.3 HADES-HADES elastic proton-proton analysis 26
2.3 ΛK_S^0 channel 28

3 Conclusions and outlook **37**

List of Figures

1.1 Scheme of the HADES detector with attached forward tracker. Graphic from [6] 13
1.2 STS2 in the maintenance position. Picture taken from [14] . . 16
1.3 Straw tubes prepared for the PANDA experiment. The picture has been taken from [15] 17

2.1 Diagram of the analyzed ΛK_S^0 process. 22
2.2 Differences between reconstructed track parameters and those provided by the event generator (ground truth) for protons reconstructed by main HADES detector (top row) and by protons reconstructed using the forward HADES detector (bottom row). The red lines present the best fit of the data using a Gaussian function with constant background. 24
2.3 Angular distributions of protons candidates selected for the 4C refit with whom the fitter converged. The top row present distributions before refit and bottom row present distributions after the refit. The last column shows χ^2 and probability distribution of the refit. 25
2.4 Distribution of reconstructed momentum for protons in the Forward Detector. The figure is obtained using data from Monte-Carlo simulations. 26
2.5 Refit results of the 4C fit to proton-proton elastic scattering channel with both protons coming from the main HADES. The data comes from Monte-Carlo simulations. The top row present distributions before refit and bottom row presents distributions after the refit. The last column shows χ^2 and probability distributions of the refit. 27

2.6 Refit results of the 4C fit to proton-proton elastic scattering channel with both protons coming from the main HADES. The data comes from HADES February 2022 run. The top row present distributions before refit and bottom row presents distributions after the refit. The last column shows χ^2 and probability distributions of the refit. 27
2.7 Differences between reconstructed track parameters and those provided by the event generator (ground truth) for protons reconstructed by main HADES detector. The red lines present the best fit of the data using a Gaussian function with constant background. 28
2.8 Differences between reconstructed track parameters and those provided by the event generator (ground truth) for π^+ (top row) and π^- (bottom row) reconstructed by main HADES detector. The red lines present the best fit of the data using a Gaussian function with constant background. 29
2.9 Distributions of momentum provided by event generator (top row) and reconstructed by Main Hades and Forward HADES detector (bottom row). 30
2.10 Probability (top row) and number of iterations (bottom row) distributions of Λ, K^0_S, primary vertex refit and full interaction refit. 32
2.11 Azimuthal and polar angle distributions of particles that decayed from the Λ candidate. Distributions before the refit are presented in top row and after the refit are shown in bottom row. 33
2.12 Azimuthal and polar angle distributions of particles that decayed from K^0_S candidate. Distributions before the refit are presented in top row and after the refit are shown in bottom row. 33
2.13 Λ and K^0_S reconstructed mass distributions before refit (top row) and after refit (bottom row). Only convergence criterion is applied. 34
2.15 Distributions of the reconstructed Λ mass with different probability of full reaction reconstruction probability P_R cuts. . . . 35
2.14 Distributions of the reconstructed Λ mass with different probability of Λ refit P_Λ cuts. 35

List of Tables

2.1 Obtained proton track resolution for the proton-proton elastic analysis. 23
2.2 Obtained track resolution for the ΛK_S^0 channel. 29
2.3 Table with number of events with particles selected and detected. 36
2.4 Table with final efficiencies of the fitter. 36

Chapter 1

Introduction

1.1 Brief overview of report structure

In sections 1.2-1.5 I will give a brief introduction to hyperons, tracking, the PANDA and the HADES experiments. The kinematic refit and the constraints that were used are explained in section 1.6. In section 2.1 I motivate why the proton-proton elastic and the ΛK_S^0 channels have been selected, then in section 2.2 I describe the analysis procedure and observations regarding using the procedure for the proton-proton elastic analysis. In section 2.3, the analysis procedure and results for the ΛK_S^0 channel are presented. In chapter 3 I present my conclusions and possible outlook for those two analyzed channels.

1.2 Hyperons and their importance

Hyperons are baryons that contain at least one strange quark s. They are hard to study experimentally (*i.a.* due to complex decay topology), and apart from a few light ones we do not know much about them. They are however very important for our understanding of physics in areas such as quark-gluon plasma [1], fundamental interactions and neutron stars. Hyperons became famous after a theoretical calculation [2] suggested that cores of neutron stars could contain hyperons. Hyperon correlations are also important for studies of the strong force [3]. Therefore it is important to develop and test ways of efficient hyperon selection and reconstruction in experiments.

1.3 The HADES experiment

The HADES (High Acceptance DiElectron Spectrometer) is a fixed target experiment at GSI Helmholtzzentrum für Schwerionenforschung in Darmstadt. It is using high energy (up to 4.5 GeV per nucleon) beams of protons and heavy ions (*e.g.* Au+Au 1.23 AGeV collisions in 2012 run [4]). For the 2022 beamtime, the detector consists of the main HADES upgraded with detectors in forward direction. The main HADES detector has a polar angle coverage from 16° to 88° and almost full coverage of the azimuthal angle. The polar angle is measured as the angle from the beamline (z-direction) and the azimuthal angle spans a plane perpendicular to the beamline (x/y plane). The Forward Tracker is capable of collecting data in the polar angle range of $0.5° - 7°$ [5]. The HADES detector with the Forward Tracker is visible in Figure 1.1.

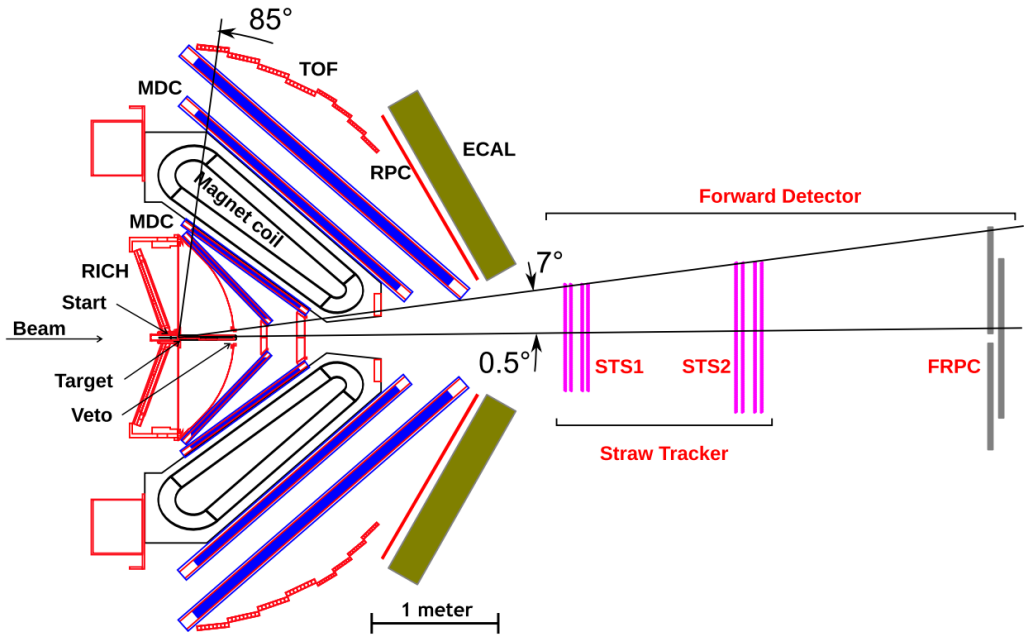

Figure 1.1: Scheme of the HADES detector with attached forward tracker. Graphic from [6]

The main HADES spectrometer consists of the following subdetectors:

- START is an Low Gain Avalanche Diode (LGAD) based detector that allows for precise time and position measurement [7]. It is used in heavy ion runs, as well as the 2022 proton-proton run, to measure beam quality. It is also part of the TOF detector system measuring the reaction time [8].

- Time of Flight (TOF) detector contains six time-of-flight hodoscopes placed in the open sectors of the toroidal magnet. Each hodoscope consists of 22 modules which in turn consist of 8 scintillation strips closed from both sides with photomultipliers [9]. Time of Flight detector has polar angle coverange of $44^\circ < \theta < 88^\circ$.

- Inner TOF (iTOF) is a detector added in 2021 that suppress empty events in HADES. It can also be use as secondary T_0 detector.

- Ring Imaging Cherenkov (RICH) is a detector that allows for electron/positron identification using Cherenkov radiation (heavier particles are not fast enough to produce such radiation).

- Multiwire Drift Chambers (MDC) is a tracking system that allows for momentum measurement.

- Pre-shower detectors for electron identification through a shower processes that they produce in the lead material of the detector.

- Resistive Plate Chambers (RPC) consist of 116 cells that are made of aluminium and two glass electrodes closed in SF_6 and $C_2H_2F_4$ gas mixture. The gas is ionized by traversing particles or traversing particle which creates an electron avalanche that is measured. It allows for time of flight calculation expanding TOF detector polar angular acceptance for $12^\circ < \theta < 45^\circ$.

- Electromagnetic Calorimeter (ECAL) measures particle energy by detection of produced Cherenkov light that is produced by shower electrons and positrons inside lead glass. It consists of 163 trapezoidal modules and offers polar angle coverage of $12^\circ - 45^\circ$ [10].

Technical details on the main HADES detector have been taken from [8].

For my analysis, the most important part is the MDC since it is capable of measuring momentum and tracking of charged particles. The fitting procedure I used takes reconstructed track parameters and adjusts them under kinematic constraints.

MDC is a tracking system consisting of four planes of a multiwire drift chamber divided into 6 trapezoidal sectors. Two of these planes are placed before and another two are placed after the powerful toroidal magnets that are capable of producing a 3.6 T magnetic field that bends trajectories of charged particles. The MDC is capable of measuring momentum with a resolution of about 1%. Each plane is of a different size in the way that the angular acceptance for every plane stays the same (between 18° and 85°). Each plane has around 98% efficiency in detecting passing particles and has an average spatial resolution between 100 µm and 130 µm. For my analysis, it is important to note that tracking in the MDC is performed through the Runge-Kutta method, so uncertainties of track parameters are not known.

1.4 The PANDA experiment and the HADES Forward Detector

The PANDA (antiProton ANnihilation at DArmstadt) will be an experiment utilizing a secondary antiproton beam of energy up to 15 GeV/c colliding with stationary target. The physics ambitions of the PANDA experiment are described in [11] and in [12].

Forward Tracker (FT) is beeing preapered for the PANDA experiment.
It will be used for momentum analysis. It will consist of 3 pairs of Forward Tracking Stations. Each station will be made of four straw tube double-layers (two one-straw deep layers glued together) [13].

Straw tube tracking planes similar to the ones prepared for PANDA have been incorporated into HADES as a Straw Tracking Stations (STS). It is divided into two modules STS1 and STS2 (see Figure 1.2) each consisting of 4 straw tubes double layers. STS1 starts around 3.34 m away from the target and consists of two horizontal and two vertical planes. STS2 starts around 0.68 m further from the target and has one vertical, one horizontal and two rotated by +45° and -45° double planes. Due to the low angle with respect to the beamline and kinematic of reactions (momentum conservation forces heavier particle to travel in the beam direction) the forward detectors detects almost only protons.

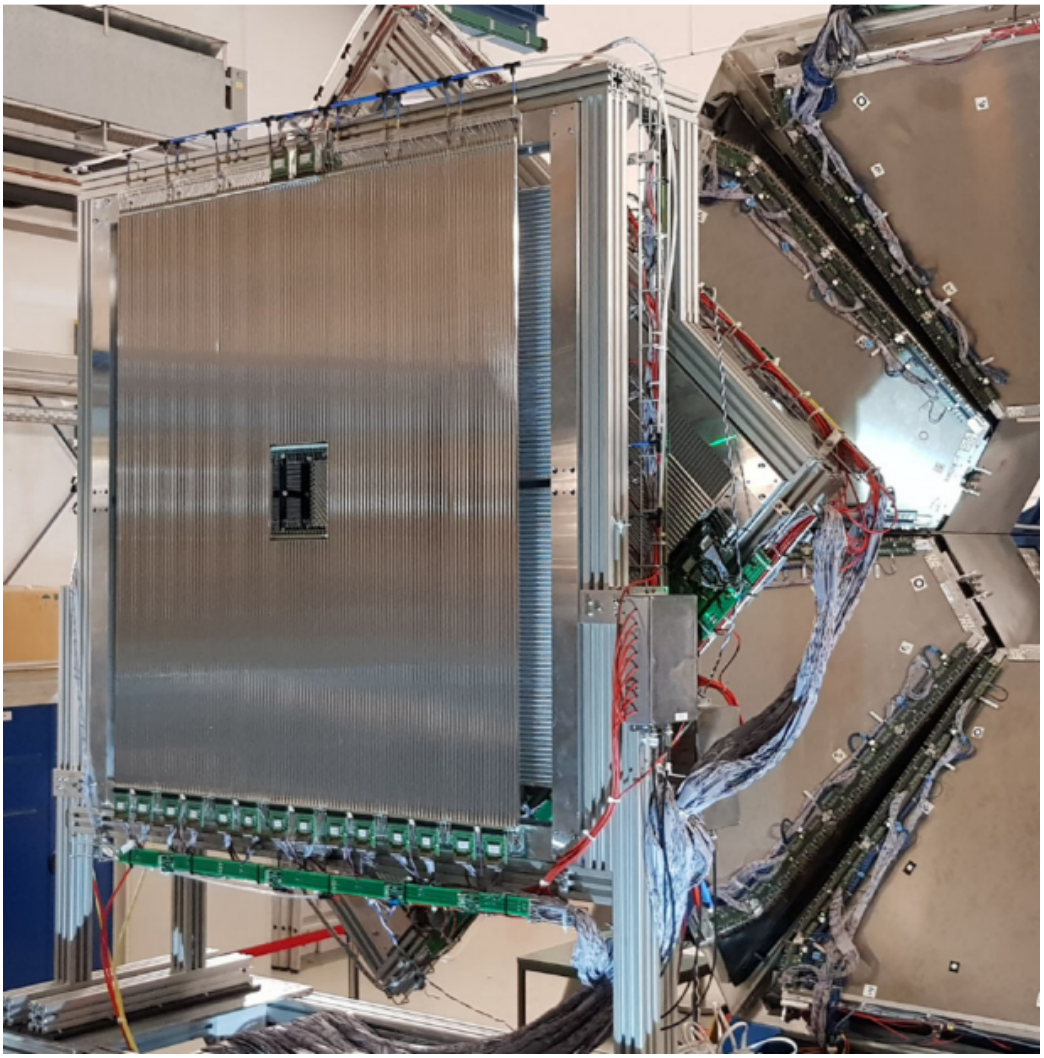

Figure 1.2: STS2 in the maintenance position. Picture taken from [14]

Each straw tube consists of an anode wire, and a cathode tube wall and is filled with Ar-CO_2 mixture. Each straw tube has 99% detection efficiency for single-hit particles. Disassembled straws are shown in Figure 1.3. Whenever charged particle passes through the tube, it ionizes gas molecules which induce an electric signal that is measured. From the electric signal and with a proper detector calibration, it is possible to calculate the minimum distance that a particle passed by from the straw wire. Knowing which straws have given rise to a signal above threshold and from the measured distances to a particle it is possible to fit the track of a particle. The STS has a spatial resolution better than 150 µm and is capable of handling hit rates up to 2 MHz.

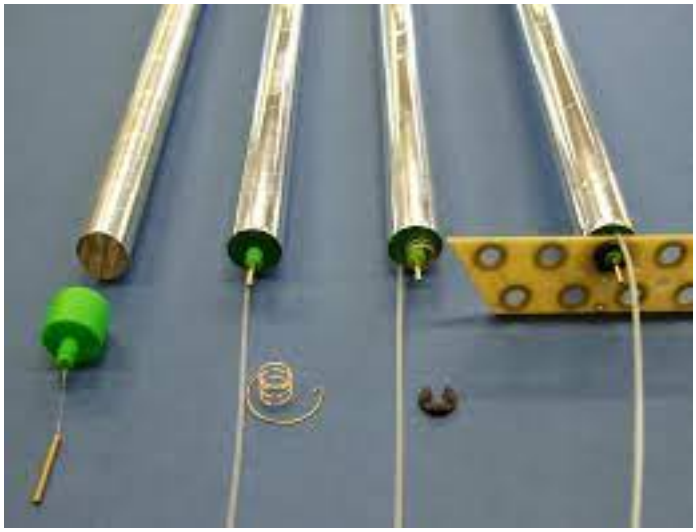

Figure 1.3: Straw tubes prepared for the PANDA experiment. The picture has been taken from [15]

.

1.5 Tracking of particles in experiments

In high-energy physics experiments that lack a magnetic field, particles move along straight trajectories. The simplest way of determining the trajectories of such particles is to measure points through which particles interacted with the detector material. This can be done using drift chambers or straw tube detectors. However fitting lines to such obtained data points is often not sufficient enough for studying particle interactions. Kinematic fitting is a process in which the resolution is improved by the use of additional constraints such as physics laws governing interactions (*e.g.* conservation laws).

1.6 Kinematic Refit

Kinematic fitting for the HADES experiment has been developed by Jana Rieger, Jenny Regina and Waleed Esmail. The algorithm uses Lagrange's multiplier method to minimize χ^2 while simultaneously satisfying one of the chosen constraints. χ^2 is calculated as:

$$\chi^2(x) = (y-x)^T V^{-1} (y-x), \tag{1.1}$$

where x denotes the measured quantities vector, y denotes the estimated fit quantities vector and V is variance-covariance matrix. So far non-diagonal elements in these matrices have not been implemented, so covariances between different variables are not included. The constraint equation uses measured x and unmeasured ξ quantities vectors:

$$g(x, \xi) = 0. \tag{1.2}$$

After applying the Lagrange multipliers minimization method to a constraint equation 1.2, one obtains:

$$\chi^2(x, \xi, \lambda) = (y-x)^T V^{-1} (y-x) + 2\lambda^T f(x, \xi), \tag{1.3}$$

where λ is a vector containing Lagrange parameters. If we expand the obtained equation 1.3 into the Taylor series around the x, ξ vectors while neglecting non-linear order terms we end up with an iterative procedure for updating variables:

$$\begin{aligned} r &= g^v + G_x^v (y - x^v), \\ S &= G_x^v V \left(G_x^v\right)^T, \\ \xi^{v+1} &= \xi^v - \left(G_\xi^T S^{-1} G_\xi\right)^{-1} G_\xi^T S^{-1} r, \\ \lambda^{v+1} &= S^{-1} \left(r + G_\xi \left(\xi^{v+1} - \xi^v\right)\right), \\ x^{v+1} &= y - V G_x^T \lambda^{v+1}, \end{aligned} \tag{1.4}$$

where G_ξ and G_x are derivative matrices of the constraint equation with respect to ξ and x. Estimated quantities vector is denoted by y.

1.6.1 Track parametrization

To construct the constraint equations, we need a description of the reconstructed track of the measured particle candidate. The track parametrisation uses the set of five variables:

- $\frac{1}{p}$- one over momentum.
- θ-polar angle.
- ϕ-azimuthal angle.
- R-closest distance from track to the beamline.
- Z-the z coordinate along the beamline that is closest to the track.

Now I will discuss some possible constraints that may be applied to the tracks for improving the resolution of the initial tracking.

1.6.2 Vertex constraint

Elementary particles emerging from an interaction originate from a point. Ideally, trajectories of the particle tracks should be intersecting each other in this point. However, due to a finite resolution of the detectors, this point will have a finite resolution. In reaction channels where at least two particles are directly detected, it is possible to slightly change the tracks of particles that they do intersect. This is referred to as constraining the tracks to a common point, *e.g.* the midpoint between the tracks. The vertex constraint might be applied to the decay of particle, in that case vertex would be a position where the decay take place. To be able to observe such a displaced vertex it is necessary that the decay would took place sufficiently far away from the interaction point. The vertex constraint is optimal to apply to the decay products of Λ and K_S^0 that decay through the weak interactions therefore they have a relatively long decay time (Λ has a lifetime of about $12.6\frac{\text{fm}}{\text{c}}$ [16]). Geometrical tracks can be parameterized by $\vec{b}$-base vector and $\vec{v}$-direction vector. They can be calculated as:

$$\begin{aligned} v_x = \sin(\theta)\cos(\phi), b_x = R\cos\left(\phi + \frac{\pi}{2}\right), \\ v_y = \sin(\theta)\sin(\phi), b_y = R\sin\left(\phi + \frac{\pi}{2}\right), \\ v_z = \cos(\theta), b_z = Z. \end{aligned} \tag{1.5}$$

Using this paremetrization, the distance between two tracks is proportional to:

$$d = (\vec{v_1} \times \vec{v_2}) \cdot \left(\vec{b_1} - \vec{b_2}\right). \tag{1.6}$$

1.6.3 4-Constraint

"Four over constraints" in the kinematic fitter is a four-momentum constraint, where we require the sum of the four-momenta of all the final-state particles to add up to the combined four-momentum of the beam and target. The latter is known with high accuracy. This constraint requires that the momenta of all final-state particles are measured.

1.6.4 3-Constraint

"Three over constraints" can be applied to broader cases, when not all particles have been detected. It requires only that the decay products of the decaying particles are known. The constraint is that the combined four-momentum of the product particles are equal to the four-momentum of a particle that decayed. The fitter returns the product particles of the decay and the decaying mother particle with adjusted parameters.

Chapter 2

Analysis

For the presented analysis, I used data taken during the latest HADES run in February 2022 and data obtained using a Monte Carlo simulation. The simulated data were obtained using the PLUTO event generator combined with the GEANT3 transport model. Data were stored in Data Summary Tapes (DSTs). During the course of this project, the DSTs contained various errors that were not resolved during the time of my work. Some of them have been found by me and are currently being fixed.

2.1 Analyzed reaction channels

I have analyzed the proton-proton elastic scattering channel, and $pp \rightarrow p\pi^+\Lambda K_S^0$ as illustrated in Figure 2.1.

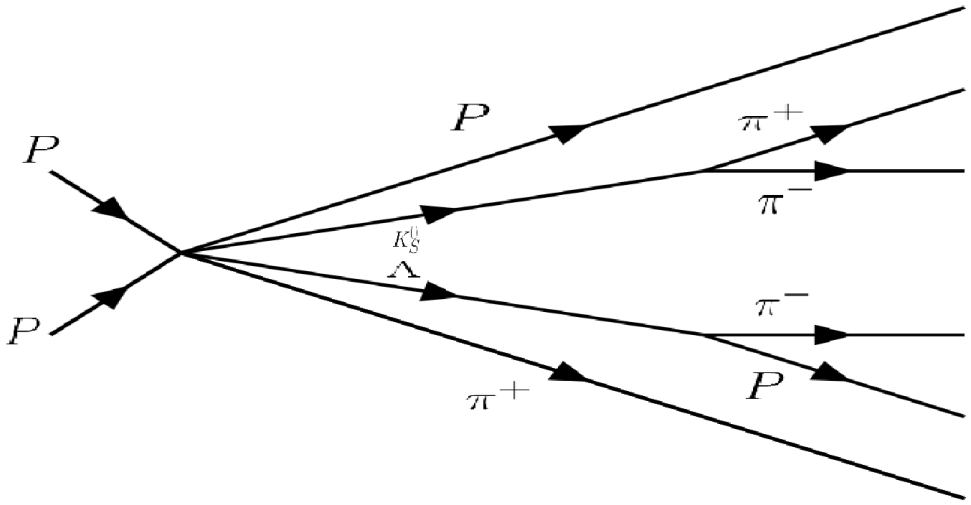

Figure 2.1: Diagram of the analyzed ΛK^0_S process.

I used the elastic proton-proton channel as a benchmark reaction. This reaction has a large cross section and therefore provides sufficient statistics. Moreover, protons are stable charged particles and no secondary vertices are to be expected. Together with the simple kinematics (two-body reaction), the elastic proton-proton channel is relatively easy to observe and to reconstruct.

The ΛK^0_S reaction channel, on the other hand, has been chosen since this channel contains long-lived particles decaying via the weak interaction. This channel provides a benchmark of the fitter in view of event topologies including secondary vertices: an important aspect for the overall hyperon physics program of HADES. In the past, the fitter has been tested for the single Λ production channel. A follow-up study with two neutral particles (Λ and K^0_S) would expand these results.

2.2 Elastic proton-proton interaction

2.2.1 Obtaining variances of parameters

Using simulated DSTs, I have selected protons that were reconstructed from the main HADES detector with the condition on mass and charge of the particles:

$$\begin{gathered} 838.272\ \frac{\mathrm{MeV}}{\mathrm{c}^2} < M < 938.272\ \frac{\mathrm{MeV}}{\mathrm{c}^2}, \\ q = +1. \end{gathered} \tag{2.1}$$

The range of the mass cut is left loose on purpose, since we wanted to keep a larger statistics and let the fitter discard improbable events. The tracks reconstructed by the forward detector were presumed to be protons. I compared reconstructed track parameters with those obtained from the event generator and I studied their differences for both the protons reconstructed by the main HADES and by those reconstructed using the forward detector. The resulting spectra were, in first order, distributed according to a Gaussian shape. The variances of the track parameters were, therefore, taken as the standard deviations of the fit using a Gaussian function with constant background. Figure 2.2 depicts the resulting plots including the fits. The obtained resolutions of the track parameters are presented in Table 2.1.

	$\frac{1}{p}\ \left[\frac{\mathrm{c}}{\mathrm{MeV}}\right]$	$\theta[^\circ]$	$\phi[^\circ]$	R [mm]	Z[mm]
HADES proton	$1.81 \cdot 10^{-4}$	0.843	0.896	8.00	9.31
Forward proton	$1.58 \cdot 10^{-5}$	$7.07 \cdot 10^{-2}$	0.952	5.14	68.7

Table 2.1: Obtained proton track resolution for the proton-proton elastic analysis.

.

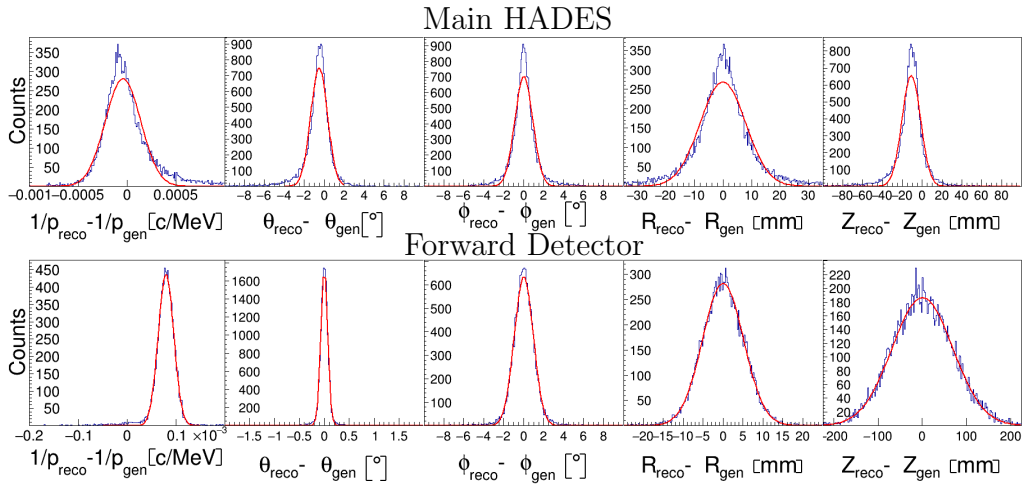

Figure 2.2: Differences between reconstructed track parameters and those provided by the event generator (ground truth) for protons reconstructed by main HADES detector (top row) and by protons reconstructed using the forward HADES detector (bottom row). The red lines present the best fit of the data using a Gaussian function with constant background.

2.2.2 Forward-main HADES elastic proton-proton analysis

Using simulated DSTs of 500100 events, I have chosen protons reconstructed using the main HADES and the Forward Tracker the same way as for obtaining variances of track parameters. In this case, however, I applied the fitter only to pairs consisting of one proton from the main HADES and one proton from the Forward Detector that satisfied polar θ and azimuthal ϕ angle cuts for the elastic proton-proton interaction proposed by Jana Rieger and Konrad Sumara:

$$\begin{aligned} 187^\circ > |\phi_{FW} - \phi_{HAD}| > 173^\circ, \\ 0.394 > \tan\theta_{FW} \cdot \tan\theta_{HAD} > 0.194. \end{aligned} \tag{2.2}$$

The cuts are based upon momentum conservation. To all pairs of protons satisfying these cuts I have applied vertex, 3C and 4C constraints. Further analysis was done with particle pairs whereby the fitter converged with a maximum of 50 iterations and with the condition that the difference in in χ^2 between subsequent iterations: $\Delta\chi^2 < 5$. The vertex and 3C fit gave unsatisfactory results with the fitter converging in only up to 5 pairs of

protons. The 4C fit converged in in bigger number of events. It's results are shown in Figure 2.3.

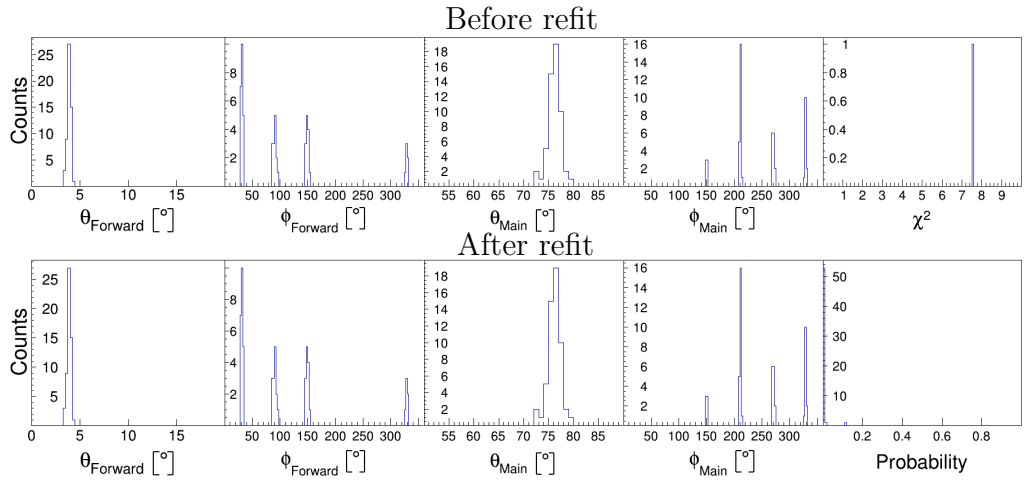

Figure 2.3: Angular distributions of protons candidates selected for the 4C refit with whom the fitter converged. The top row present distributions before refit and bottom row present distributions after the refit. The last column shows χ^2 and probability distribution of the refit.

Figure 2.4 shows the distribution of reconstructed momenta of the protons detected in the forward HADES detector. I observed that large portion of of reconstructed protons had momentum equal to zero. Since this feature could not be resolved during this project, I decided not to use data collected by Forward Detector.

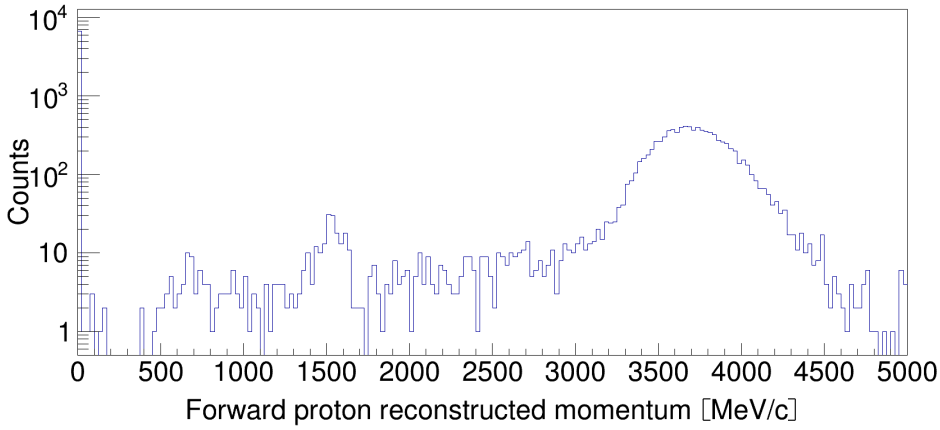

Figure 2.4: Distribution of reconstructed momentum for protons in the Forward Detector. The figure is obtained using data from Monte-Carlo simulations.

2.2.3 HADES-HADES elastic proton-proton analysis

After identifying challenges associated with the momentum reconstruction of protons in the forward HADES detector, I decided to perform a further study for events in which both protons were detector by the main HADES setup. I applied the same conditions as in the Forward-HADES case, but with the slightly changed elastic conditions:

$$\begin{aligned} 182^\circ > |\phi_{HAD1} - \phi_{HAD2}| > 178^\circ \\ 0.309 > \tan\theta_{HAD1} \cdot \tan\theta_{HAD2} > 0.279 \end{aligned} \tag{2.3}$$

I have studied both 3C and 4C fits. Both fits gave similar results. The 4C fit for simulated data results are presented in Figure 2.5. Figure 2.6 shows the results of the 4C fit for data taken from the February 2022 runs. In all cases presented in Figures 2.3, 2.5 and 2.6, we observe discrete anomalies in the spectra. These features are yet not fully understood and require further investigations before one can draw any conclusion on the performance of the fitter itself.

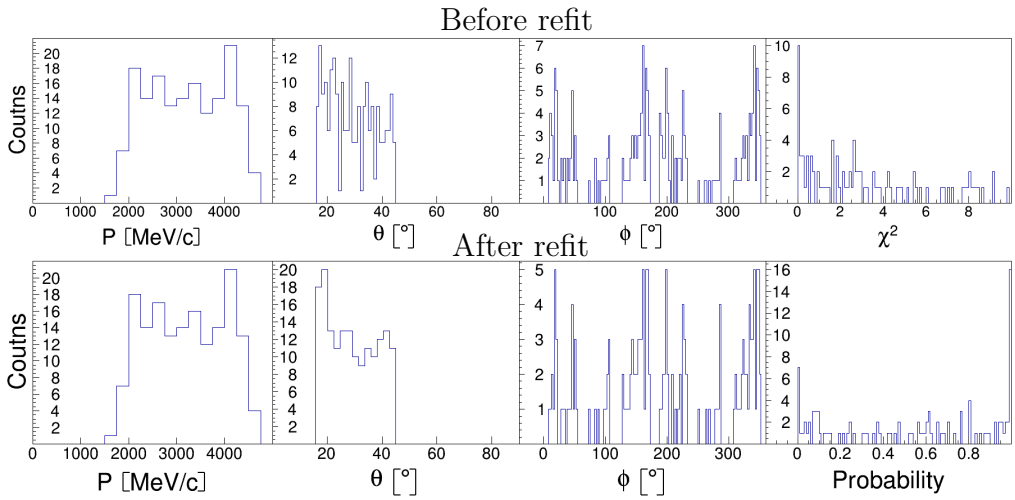

Figure 2.5: Refit results of the 4C fit to proton-proton elastic scattering channel with both protons coming from the main HADES. The data comes from Monte-Carlo simulations. The top row present distributions before refit and bottom row presents distributions after the refit. The last column shows χ^2 and probability distributions of the refit.

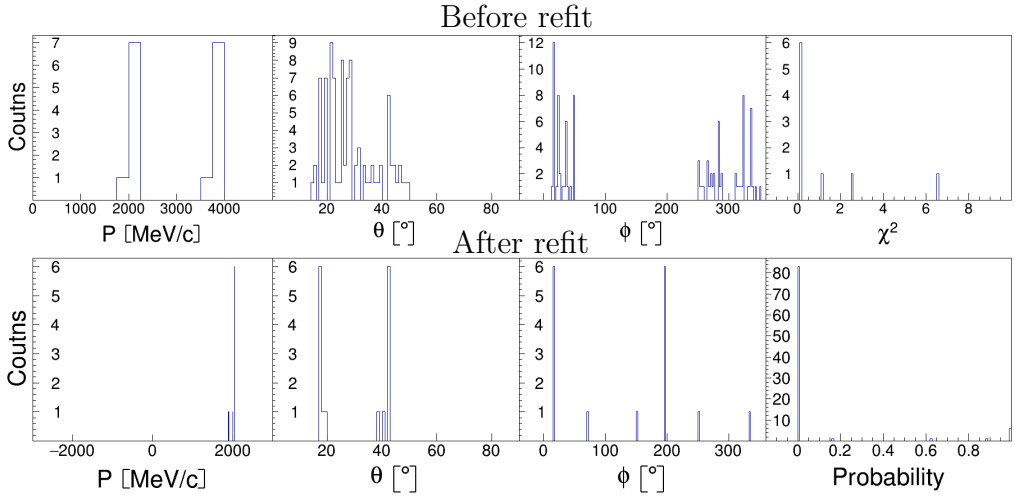

Figure 2.6: Refit results of the 4C fit to proton-proton elastic scattering channel with both protons coming from the main HADES. The data comes from HADES February 2022 run. The top row present distributions before refit and bottom row presents distributions after the refit. The last column shows χ^2 and probability distributions of the refit.

2.3 ΛK_S^0 channel

For the analysis of the ΛK_S^0 channel, new DSTs based on simulated data have been prepared. For obtaining variances I used the same method (except the forward proton case and the Z parameter of π^-) of plotting differences of reconstructed and simulated values of track parameters and fitting Gaussian function with constant background. Due to the difference in detector response of charged pions and protons it is required to calculate track parameters resolutions separately for protons, π^+ and π^-. The results are visible in Figures 2.7 and 2.8. Obtained resolutions of track parameters are presented in the Table 2.2.

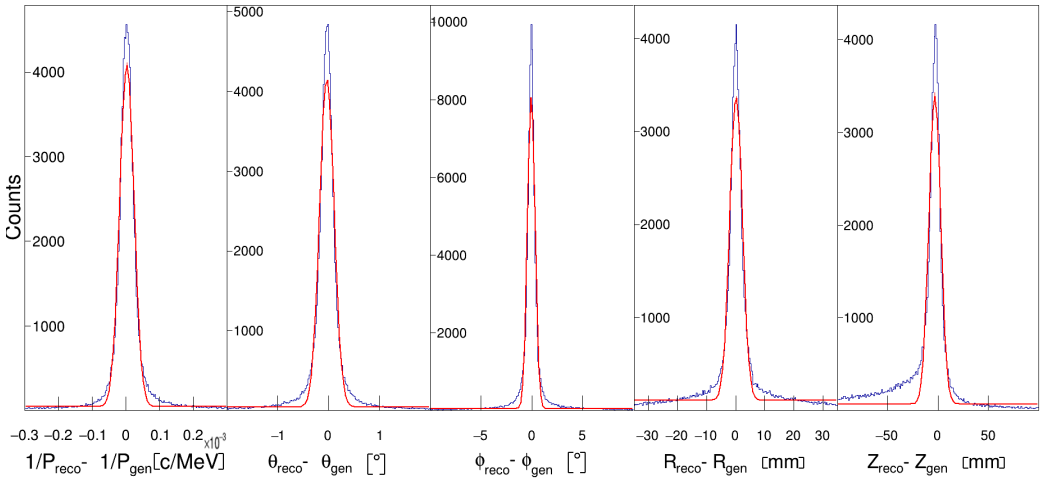

Figure 2.7: Differences between reconstructed track parameters and those provided by the event generator (ground truth) for protons reconstructed by main HADES detector. The red lines present the best fit of the data using a Gaussian function with constant background.

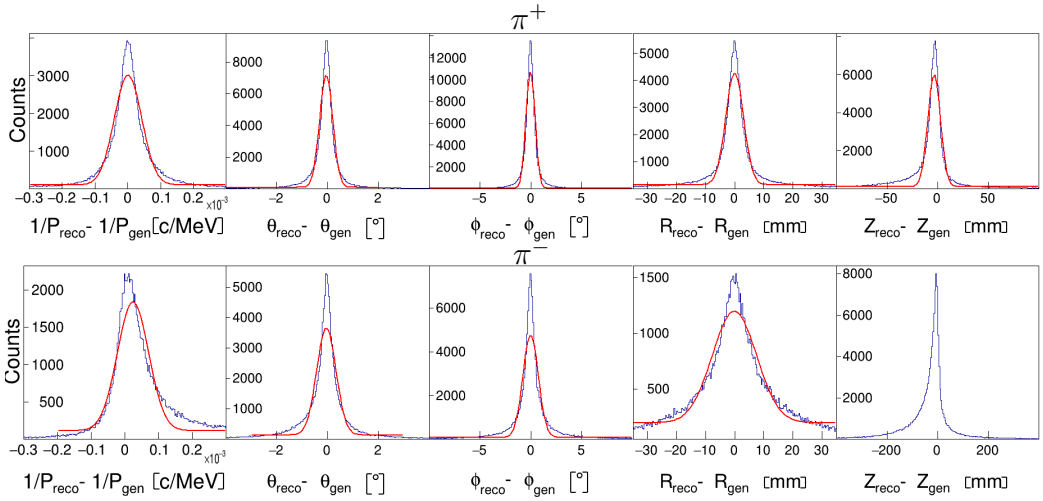

Figure 2.8: Differences between reconstructed track parameters and those provided by the event generator (ground truth) for π^+ (top row) and π^- (bottom row) reconstructed by main HADES detector. The red lines present the best fit of the data using a Gaussian function with constant background.

	$\frac{1}{p}$ $[MeV^{-1}]$	θ[°]	ϕ[°]	R [mm]	Z[mm]
HADES proton	$2.14 \cdot 10^{-5}$	0.143	0.372	2.18	5.89
π^+	$4.20 \cdot 10^{-5}$	0.260	0.444	3.07	6.22
π^-	$4.64 \cdot 10^{-5}$	0.381	0.758	7.61	40.0

Table 2.2: Obtained track resolution for the ΛK_S^0 channel.

The variance of the Z parameter in the π^- case was estimated with full-width-at-half-maxi mum (FWHM), using the formula:

$$\sigma = \frac{\text{FWHM}}{2\sqrt{2\log 2}}. \tag{2.4}$$

The advantage of using the FWHM is that is it does not require a fit to extract the parameter.

There are visible problems with the momentum reconstruction of the forward proton candidates. All of the forward detector protons are reconstructed with four-momentum equal to the rest mass of a proton. This can be seen in the Figure 2.9. Therefore I decided not to use protons from the forward detector in further analysis.

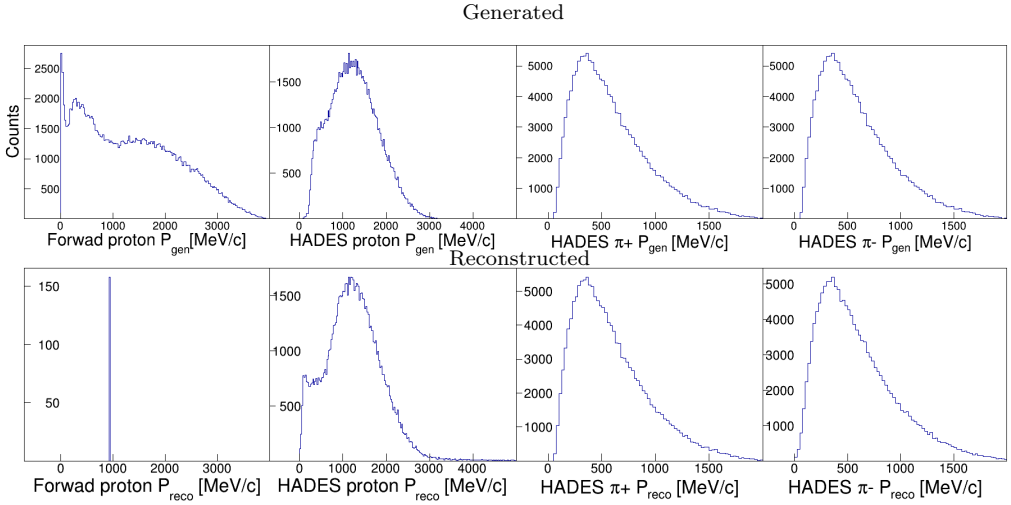

Figure 2.9: Distributions of momentum provided by event generator (top row) and reconstructed by Main Hades and Forward HADES detector (bottom row).

Analysis procedure and Monte Carlo Truth matching
I have made mass cuts on protons and pions:

$$\begin{aligned} 838.272\frac{\text{MeV}}{\text{c}^2} < M_p < 1038.272\frac{\text{MeV}}{\text{c}^2}, \\ 39.57\frac{\text{MeV}}{\text{c}^2} < M_{\pi^{+/-}} < 239.57\frac{\text{MeV}}{\text{c}^2}. \end{aligned} \tag{2.5}$$

The events analyzed were those where at least 2 protons, 2 π^+ and 2 π^- have been detected. I performed the fitting separately for all possible protons and π^- for the Λ vertex. Once the fitter converged, I stored the probability of the fit and pointer to the particles used as input for refit. The same procedure I applied to the K^0_S vertex and the primary vertex of the interaction by combining the π^+ and proton.

I selected particles that give the best probability of the full reaction (simultaneously I evaluate whether two of the used protons, π^+ and π^- are different from one another). The probability of the entire reaction P_R being true is approximated by:

$$P_R = P_\lambda \cdot P_{K^0_S} \cdot P_{prim}. \tag{2.6}$$

With the data taken from the MC simulations, I tested whether the selected tracks indeed originated from the generated ones (MC-truth matching).

Results

I have made the analysis using the vertex fit constraint with a total of 5000100 events, with the requirement that the fitter converged with a maximum of 10 iterations and difference in χ^2 between subsequent iterations smaller than one: $\Delta\chi^2 < 1$. The resulting probability and plots of the number of iterations are visible in Figure 2.10.

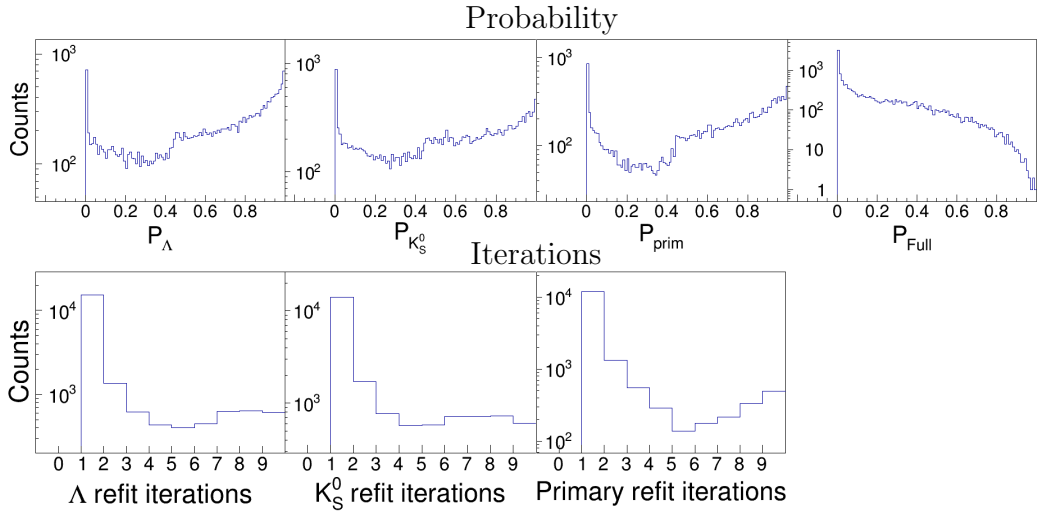

Figure 2.10: Probability (top row) and number of iterations (bottom row) distributions of Λ, K^0_S, primary vertex refit and full interaction refit.

The azimuthal and polar angles distributions of the best combination of particles before and after the refit are shown on the Figures 2.11 and 2.12.

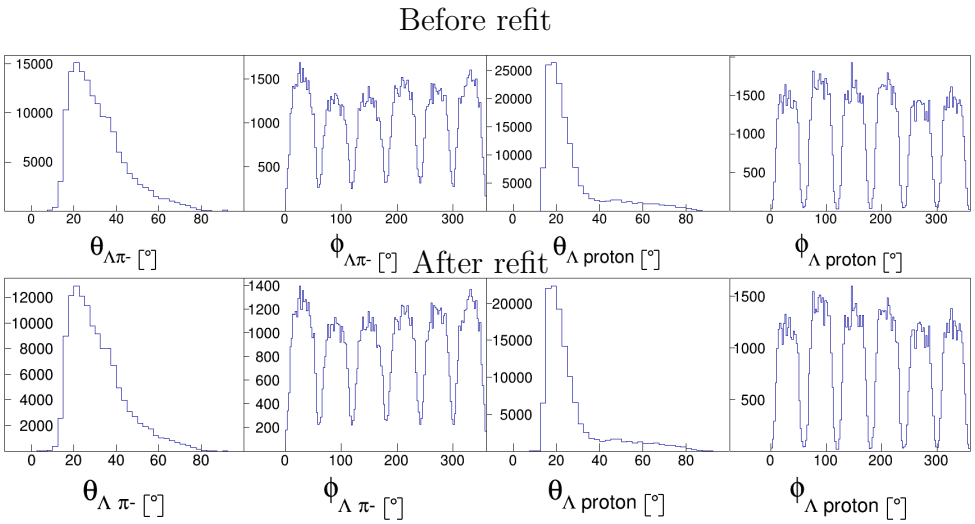

Figure 2.11: Azimuthal and polar angle distributions of particles that decayed from the Λ candidate. Distributions before the refit are presented in top row and after the refit are shown in bottom row.

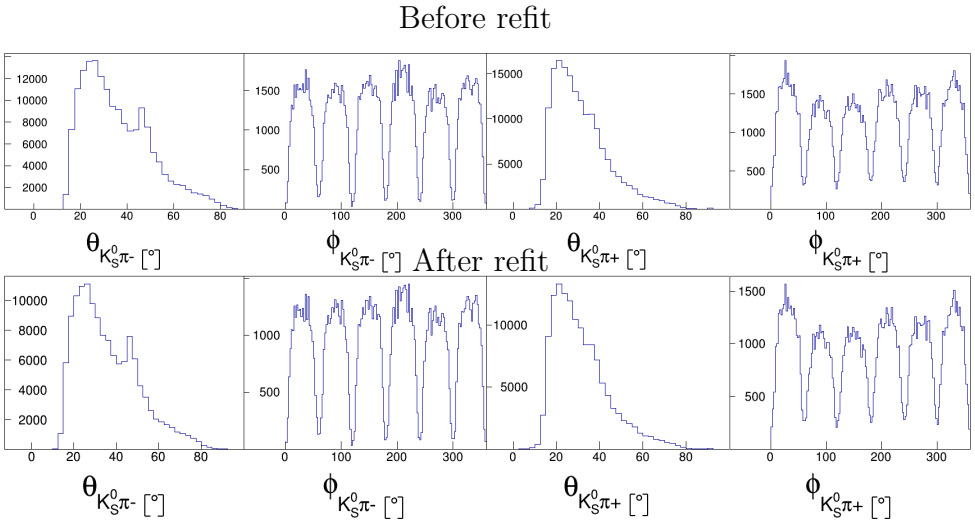

Figure 2.12: Azimuthal and polar angle distributions of particles that decayed from K_S^0 candidate. Distributions before the refit are presented in top row and after the refit are shown in bottom row.

Figure 2.13 depicts the results of reconstructed Λ and K_S^0 masses for events with the requirement that the fitter converged.

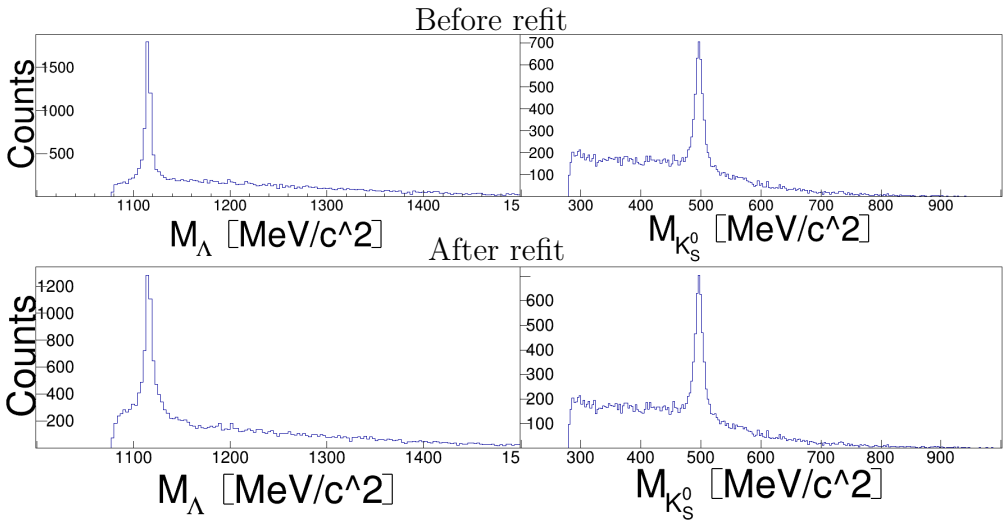

Figure 2.13: Λ and K_S^0 reconstructed mass distributions before refit (top row) and after refit (bottom row). Only convergence criterion is applied.

Testing the kinematic fitter ability to select Λ decay particles. In the future, the kinematic fitting procedure might be used as a tools to identify events with displaced vertices. For testing the ability of the vertex fit to select Λ events, I analyzed particles selected by the fitter with cuts on the probability of the Λ decay (particles were still selected with the condition of maximizing the total reaction probability). Figure 2.14 shows the results for the reconstructed mass spectrum.

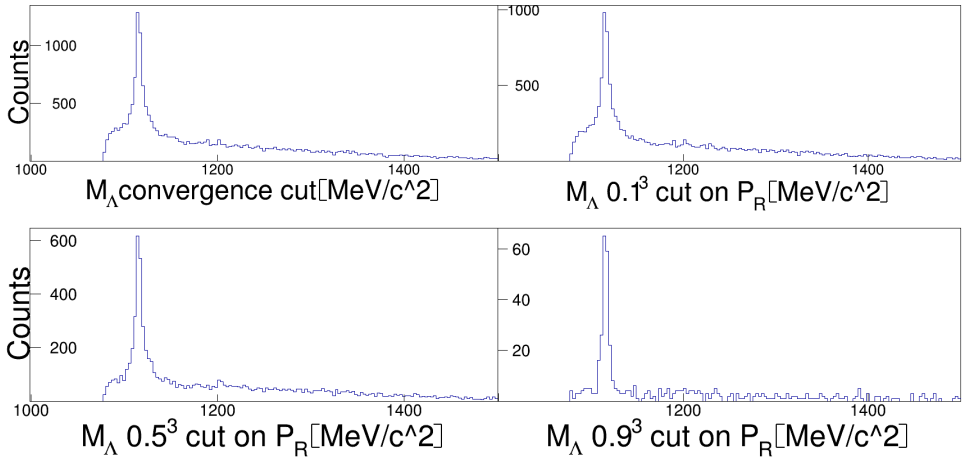

Figure 2.15: Distributions of the reconstructed Λ mass with different probability of full reaction reconstruction probability P_R cuts.

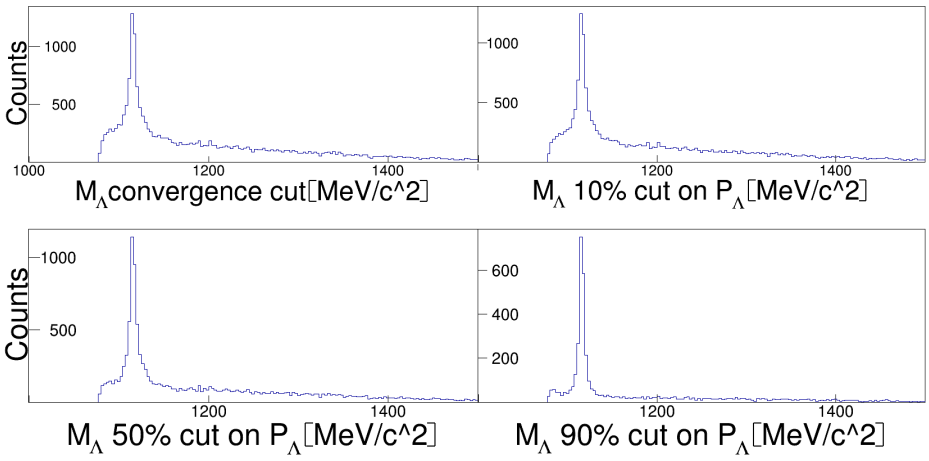

Figure 2.14: Distributions of the reconstructed Λ mass with different probability of Λ refit P_Λ cuts.

Figure 2.15 shows the reconstructed Λ mass distribution whereby different cuts were applied to the whole interaction probability calculated from equation 2.6. Table 2.3 summarizes the number of detected and selected events. Events where Λ has been detected are counted if at least one proton and one π^- that comes from Λ decay has been detected by the main HADES. Similar for K^0_S detected events. Primary events detected are counted if at least one proton and π^+ coming from the beam interaction point have been

detected in the main HADES. Events are counted as matched if at least one of each Λ, K^0_S and primary fit have converged and the particles selected by the analysis procedure comes from Λ, K^0_s interaction. Table 2.4 shows the obtained selection efficiencies for selecting Λ, K^0_S and primary particles. The efficiencies have been normalized with respect to the total number of events for which the various particles have been detected.

All events	5000100
events with all particles detected	2630
events with all particles matched	99
events with Λ particles detected	11521
events with Λ particles matched	3424
events with K^0_S particles detected	11149
events with K^0_S particles matched	3212
events with primary particles detected	10445
events with primary particles matched	3166

Table 2.3: Table with number of events with particles selected and detected.

Λ particles selection efficiency	29.7%
K^0_S particles selection efficiency	28.8%
Primary particles selection efficiency	30.3%
Entire interaction selection efficiency	3.76%

Table 2.4: Table with final efficiencies of the fitter.

Chapter 3

Conclusions and outlook

The results of the proton-proton elastic refit need further testing with new DSTs. It is likely that the main problem is associated with the momentum reconstruction of protons registered by the forward detector. Results from HADES-HADES simulations and data may suggest that, there are problem with the Forward HADES proton reconstruction.
On the other hand ΛK_S^0 analysis gave very good results. Apart from the momentum reconstruction in the forward detector, all three fits gave satisfactory results. Furthermore, it was shown that fitter is capable of performing Λ selection and significantly lowering combinatorial background. It is also important to note that the distribution of track parameters does not change significantly after applying the fitting procedure, this means that the fitter does not force the wrong particle tracks into tracks that satisfy our conditions, but it just slightly adjusts good particles parameters.
The probability distributions are not perfectly flat and even increase towards higher values. This can be observed clearly in Figure 2.10 and it could imply that the variances of the parameters have been overestimated. The fitter may have modified good particle tracks more than it is allowed to do. Note that the total refit probability distribution decreases with increasing probabilities. This could mean that the probability distributions of Λ, K_S^0 and primary refit are highly correlated.
It is possible that a large variance of the Z track parameter in the forward detector can be caused by not optimal track parametrization. Even a small difference in polar or azimuthal angle may yield huge changes in track position since forward detector is far away from a target.

Outlook

- It is advised to investigate the fitting with different constraints in the ΛK_S^0 channel.
- When new DSTs for elastic reactions are available, it would be interesting to perform the fitting procedure once again in the proton-proton elastic channel, to test how the fitting works for tracks in the forward detector in a controlled channel with well-defined kinematics.
- For hyperon identification using the kinematic fitter there is further quantitative testing needed, such as signal-to-background ratio calculations in the mass histograms in Figures 2.9 and 2.15 to quantify the improvement.
- It might be also interesting to test how the fitter is working when it is given different track parametrization for tracks provided by the forward detector.

Bibliography

[1] Francesco Becattini and Michael A. Lisa. "Polarization and Vorticity in the Quark–Gluon Plasma". In: *Annual Review of Nuclear and Particle Science* 70.1 (Oct. 2020), pp. 395–423. DOI: 10.1146/annurev-nucl-021920-095245. URL: https://doi.org/10.1146%2Fannurev-nucl-021920-095245.

[2] V. A. Ambartsumyan and G. S. Saakyan. "The Degenerate Superdense Gas of Elementary Particles". In: *Sov. Astron.* 4 (Oct. 1960), p. 187.

[3] ALICE Collaboration. "Unveiling the strong interaction among hadrons at the LHC". In: *Nature* 558 (Dec. 2020), pp. 232–238. DOI: https://doi.org/10.1038/s41586-020-3001-6.

[4] Behruz Kardan. "Collective flow measurements with HADES in Au+Au collisions at 1.23A GeV". In: *Nuclear Physics A* 967 (Nov. 2017), pp. 812–815. DOI: 10.1016/j.nuclphysa.2017.05.026.

[5] Narendra Rathod et al. "Hyperon Studies and Development of Forward Tracker for HADES Detector". In: *Acta Physica Polonica B* 51 (Jan. 2020), p. 239. DOI: 10.5506/APhysPolB.51.239.

[6] HADES collaboration and PANDA@HADES collaboration. "Production and electromagnetic decay of hyperons: a feasibility study with HADES as a phase-0 experiment at FAIR". In: *The European Physical Journal A* 57.4 (Apr. 2021), p. 138. ISSN: 1434-601X. DOI: 10.1140/epja/s10050-021-00388-w. URL: https://doi.org/10.1140/epja/s10050-021-00388-w.

[7] W. Krüger et al. "LGAD technology for HADES, accelerator and medical applications". In: *Nuclear Instruments and Methods in Physics Research Section A: Accelerators, Spectrometers, Detectors and Associated Equipment* 1039 (2022), p. 167046. ISSN: 0168-9002. DOI: https://doi.org/10.1016/j.nima.2022.167046. URL: https://www.sciencedirect.com/science/article/pii/S0168900222004697.

[8] The HADES collaboration. "The high-acceptance dielectron spectrometer HADES". In: *The European Physical Journal A* 41.2 (July 2009), pp. 243–277. DOI: 10.1140/epja/i2009-10807-5. URL: https://doi.org/10.1140%2Fepja%2Fi2009-10807-5.

[9] N. V. Rabin, D. A. Vasil'ev, and S. V. Vladimirov et. al. "A time-of-flight measurement system for the HADES wide-aperture dielectron spectrometer". In: *Instruments and Experimental Techniques* 43.4 (July 2000), pp. 435–452. ISSN: 1608-3180. DOI: 10.1007/BF02758944. URL: https://doi.org/10.1007/BF02758944.

[10] Petr Chudoba et al. "Commissioning of the electromagnetic calorimeter ECAL of the HADES experiment". In: Sept. 2020.

[11] Gianluigi Boca. "The PANDA experiment: Physics goals and experimental setup". In: *EPJ Web of Conferences* 72 (May 2014), p. 00002. DOI: 10.1051/epjconf/20147200002.

[12] "The PANDA Physics Program: Strangeness and more". In: Oct. 2015. URL: https://panda.gsi.de/publication/pa-pro-2015-012.

[13] PANDA Collaboration. *Technical Design Report for the Panda Forward Spectrometer Calorimeter*. 2017. DOI: 10.48550/ARXIV.1704.02713. URL: https://arxiv.org/abs/1704.02713.

[14] HADES collaboration and PANDA@HADES collaboration. "Production and electromagnetic decay of hyperons: a feasibility study with HADES as a phase-0 experiment at FAIR". In: *The European Physical Journal A* 57.4 (Apr. 2021), p. 138. DOI: 10.1140/epja/s10050-021-00388-w. URL: https://doi.org/10.1140/epja/s10050-021-00388-w.

[15] P. Gianotti et al. "The Straw Tube Trackers of the PANDA Experiment". In: (2013). DOI: 10.48550/ARXIV.1307.4537. URL: https://arxiv.org/abs/1307.4537.

[16] ALICE Collaboration. "Suppression of $\Lambda(1520)$ resonance production in central Pb-Pb collisions at $\sqrt{s_{NN}} = 2.76$ TeV". In: *Physical Review C* 99.2 (Feb. 2019). DOI: 10.1103/physrevc.99.024905. URL: https://doi.org/10.1103%5C%2Fphysrevc.99.024905.